Title	Three-dimensional Cauchy-condition surface method to identify the shape of the last closed magnetic surface in the Large Helical Device
Author(s)	Itagaki, Masafumi; Maeda, Tadaaki; Ishimaru, Takeshi et al.
Citation	Plasma Physics and Controlled Fusion, 53(10), 105007 https://doi.org/10.1088/0741-3335/53/10/105007
Issue Date	2011-10
Doc URL	https://hdl.handle.net/2115/47274
Rights	This is an author-created, un-copyedited version of an article accepted for publication in Plasma Physics and Controlled Fusion. IOP Publishing Ltd is not responsible for any errors or omissions in this version of the manuscript or any version derived from it. The definitive publisher authenticated version is available online at 10.1088/0741-3335/53/10/105007.
Type	journal article
File Information	PPCF53-10_105007.pdf

Three-dimensional Cauchy-condition surface method to identify the shape of the last closed magnetic surface in the Large Helical Device

Masafumi ITAGAKI[1*], Tadaaki MAEDA[1], Takeshi ISHIMARU[1], Gaku OKUBO[1],

Kiyomasa WATANABE[2], Ryosuke SEKI[2], Yasuhiro SUZUKI[2]

[1]Graduate School of Engineering, Hokkaido University,

Kita 13, Nishi 8, Kita-ku, Sapporo 060-8628, Japan

[2]National Institute for Fusion Science, Toki 509-5292, Japan

This paper contains
22 pages of text,
3 tables and
9 figures.

*E-mail: itagaki@qe.eng.hokudai.ac.jp

Abstract

Kurihara’s Cauchy condition surface (CCS) method, originally developed for axisymmetric tokamak plasma, has been expanded to reconstruct the 3-D magnetic field profile outside the non-axisymmetric plasma in the Large Helical Device (LHD). The boundary integral equations (BIE) in terms of 3-D vector potential for magnetic field sensors, flux loops and points along the CCS are solved simultaneously. In the BIE for a flux loop, the portions related to the fundamental solution are integrated along the loop. The rotational symmetry of the plasma is incorporated into the formulation to reduce the number of unknowns. The reconstructed magnetic field caused only by the plasma current agree fairly well with the reference solution for the LHD, while a good agreement is observed when adding the coil current effect to the magnetic field. The magnetic field line tracing using the reconstructed field indicates the plasma boundary (the outer surface of the stochastic region) precisely and the last closed magnetic surface agrees fairly well with the reference one.

Keywords: nuclear fusion, plasma boundary, last closed magnetic surface, Cauchy condition surface method, magnetic sensor, vector potential, vacuum field, boundary integral equation

PACS numbers: 28.52.-s, 28.52.Av., 52.55.-s, 52.55.Hc

1. Introduction

To know the boundary shape or the last closed magnetic surface (LCMS) of the plasma in a nuclear fusion device is important for the control of its operation and for diagnostic purposes as well. As the plasma temperature in such a device is extremely high, it is almost impossible to place any sensor inside the plasma. Usually, the plasma boundary shape is indirectly estimated with the aid of computing from signals of magnetic sensors located outside the plasma.

Strait et al. [1] widely reviewed the measurement techniques for magnetic diagnostics and the analytic methods for plasma boundary shape identifications. One method [2, 3] uses a small number of current “filaments” at fixed positions within the plasma domain. The currents in these filaments are then computed in such a way that one obtains the best fit to the measured magnetic fluxes and fields. Instead of such filaments, Feneberg et al. [4] assumed a “control surface” inside the plasma. The current density distribution on the surface is expressed as a sum of Fourier modes. Hofmann and Tonetti [5] proposed a method based on finite element basis functions to represent the plasma current distribution. Kurihara [6] proposed the Cauchy condition surface method, which has been applied for the JT-60 of the Japan Atomic Energy Agency (JAEA) [6, 7]. Here, the Cauchy condition surface (CCS), where both the Dirichlet and the Neumann conditions are unknown, is hypothetically placed in a domain that can be supposed to be inside the plasma. In the analysis, no plasma current is assumed outside this CCS, where in reality the plasma current does exist.

The works mentioned above focus mainly on tokamaks, i.e., axisymmetric plasmas, so that the analyses can be made in a 2-dimensional (2-D), r-z system. On the other hand, 3-D analyses are required for non-axisymmtric plasma, e.g., in a helical type device such as the Large Helical Device (LHD) of the National Institute for Fusion Science (NIFS), Japan. Even in tokamaks, 3-D considerations are required in some situations caused by perturbations during their operation [8, 9].

In a helical-type device such as the LHD, it is important to consider the following characteristics of the plasma current:

(i) The dominant plasma current is the so-called Pfirsch-Schülter current, the average of which over a magnetic surface is zero. However, this current still has a 3-D profile.

(ii) The plasma current itself is much weaker than the toroidal current in a tokamak device.

It is therefore difficult to apply most of the simplified methods quoted above, e.g., the filament method [2, 3], to the plasma in a helical-device. Among them, however, the CCS method [6] has a rigorous mathematical background (see the Appendix) that is applicable to 3-D problems.

The present work is an extension of the CCS method to non-axisymmetric, 3-D fusion plasma. Kurihara's CCS method is based on a 2-D boundary integral equation (BIE). To expand the method to a 3-D space, one needs to use a 3-D integral equation. Some examples of 3-D integral formulations are found in the literatures [10, 11, 12, 13]. Chance [10] combined the fundamental solution (Green's function) with the toroidal symmetry part of the scalar potential to simplify the BIE. The integral equation found in the paper by Atanasiu et al. [11] is not an exact form of the BIE, which has both the fundamental solution and its derivative. However, it also describes toroidal symmetric plasmas. Hirshman et al. [12] described a formulation of a magnetic diagnostic response function for a 3-D stellarator plasma, where the plasma responses were reformulated in terms of a surface current using the virtual-casing principle. Pustovitov [13] showed the BIE that is described in terms of the magnetic field as a vector quantity on the plasma surface.

In the present work, the BIE is written in terms of vector potential to deal with both magnetic field and flux loop signals. Differentiating the fundamental solution ϕ_i^* for the Laplace equation, one has the BIE for a magnetic field sensor (see equation (6)), while the BIE for a flux loop (equations (8a) and (8b)) is obtained by integrating ϕ_i^* along the loop. Further, the BIEs for points on the CCS (equation (5)) are required as constraints. These three types BIEs are solved simultaneously.

To solve this 3-D inverse problem is quite challenging. In a typical 2-D CCS analysis, as shown in Table 1, the number of unknowns is 12 [7] and then the condition number of the solver matrix is about 10^6, which is not large. A 3-D CCS analysis, on the other hand, consumes a huge number of unknowns. In the test calculation that will be shown in Section 3, 48 boundary elements and then 2592 unknowns were required even when 10-fold rotational symmetry was considered. In this case the condition number exceeds 10^{15}, i.e., the problem becomes very ill-conditioned. The authors had to introduce the Tikhonov regularization, which will be described in Section 2.5, so that the condition number was reduced to about 10^7.

Table 1 Examples of 2-D and 3-D analyses

	2-D CCS method	3-D CCS method (*1)
Governing equation	Grad-Shafranov equation	3-D Poisson equation
Unknowns to be solved	Magnetic flux function ψ (Scalar surface function)	Vector potential $\mathbf{A} = \left(A_x, A_y, A_z\right)$
Number of boundary elements	3	48
Number of unknowns	12	2592
Condition number	$\sim 10^6$	$>10^{15}$ (*2) (Ill-conditioned)

(*1) 10-fold rotational symmetry was considered.

(*2) Reduced to $\sim 10^7$ with the aid of the Tikhonov regularization

The unknown to be solved in the 2-D CCS method is a scalar function ψ, the magnetic flux function that satisfies the Grad-Shafranov equation. This scalar function is at the same time a magnetic surface function that satisfies $\mathbf{B} \cdot \nabla \psi = 0$. It is given by $\psi = rA_\varphi$, where A_φ is the toroidal component of vector potential. Unfortunately in a non-axisymmetric 3-D problem, no such simple mathematical expression has been found yet for the surface function. Consequently, in the 3-D CCS method proposed here, one needs to solve the 3-D Poisson equation in terms of the three components of vector potential. This is also one of the reasons why so many unknowns are required for the 3-D CCS analysis.

In section 2, one describes the formulation of the present 3-D CCS method together with some related numerical techniques. Numerical examples are shown in Section 3 to demonstrate the validity of the present formulation.

2. Three-dimensional CCS method

In the 3-D version of the CCS method proposed here, the CCS (Γ_{CCS}) is assumed to have a torus shape and to be located in the actual plasma region in 3-D space, as illustrated in figure 1. In the present work the Dirichlet condition and the Neumann condition along the CCS are the vector potential and its derivative, respectively, while they were the magnetic flux and its derivative in the conventional 2-D CCS method [6, 7].

The torus shape CCS is divided into a certain number of boundary elements, each of which has 9 nodal points. The first step of the analysis is to obtain the values of the Dirichlet and Neumann conditions at each nodal point in such a way that they will be consistent with the magnetic sensor signals. For this purpose, one solves the set of boundary integral equations for a vacuum field in the same way as that adopted in the 2-D CCS method calculation.

Figure 1 Extention of CCS method to a 3-D system

2.1 Hypothetical assumption of vacuum field

One here assumes mathematically that there is no plasma current, i.e., vacuum everywhere outside the CCS. Instead of the actual plasma current, the boundary conditions on the hypothetical CCS plays the same role in giving the vector potential outside the plasma. That is, at any point outside the plasma boundary the vector potential calculated under this assumption is exactly the same as the vector potential caused by the existence of the plasma current. The proof for this is given in the Appendix.

2.2 Use of Cartesian coordinate system

In a 3-D Cartesian coordinate system, the vector Laplacian applied to the vector potential $\boldsymbol{A}$ in the Poisson equation has the simple relationship

$$(\nabla^2 \boldsymbol{A})_k = \nabla^2 A_k \qquad (k = x,\ y,\ z)\,. \tag{1}$$

That is, the vector Laplacian can be given as the set of the scalar Laplacians for each Cartesian scalar component. Because of this, the authors adopt a 3-D Cartesian coordinate system to realize a boundary-only integral formulation. Otherwise the BIE would include domain integral terms.

2.3 Sensor signals described using vector potential

Figure 2 illustrates the location of three types of magnetic sensors: the field sensors, the flux loops in the toroidal direction and the ones in the poloidal direction. Due to the adoption of a Cartesian coordinate system, all of the sensor signals are described using A_x, A_y and A_z.

Figure 2 Image of magnetic sensor locations

In this work, the magnetic field sensor signals are assumed to be given in terms of B_r, B_φ and B_z. They are described following $\mathbf{B} = \nabla \times \mathbf{A}$ with $\mathbf{A}$ expressed in Cartesian coordinates.

For a flux loop set in the toroidal direction, the magnetic flux can be described as

$$\psi^{(Tor)} = \int_C R A_\varphi d\varphi\ . \tag{2a}$$

Here R and φ denote the major radius of the loop and the toroidal angle, respectively. Similarly, the magnetic flux for a loop set at the toroidal angle φ in the poloidal direction can be given by

$$\psi^{(Pol)} = \int_C a A_\theta d\theta \tag{2b}$$

where a means the radius of the poloidal loop and θ the poloidal angle.

2.4 Boundary integral equations

It is well known that the BIE corresponding to the 3-D scalar Laplace equation $\nabla^2 A = 0$ is written in the form [14]

$$c_i A_i = \int_\Gamma \left(\phi_i^* \frac{\partial A}{\partial n} - A \frac{\partial \phi_i^*}{\partial n} \right) d\Gamma \tag{3}$$

with the fundamental solution ϕ_i^* that satisfies the equation with the Dirac delta function

$$\nabla^2 \phi_i^* + \delta_i = 0\ . \tag{4}$$

The parameter c_i in equation (3) takes the value of 1/2 for a smooth boundary Γ while it is 1.0 within the domain surrounded by the boundary.

The BIE corresponding to a point i on the CCS or the BIE corresponding to each sensor location i can be given as follows, by applying equation (3) for each situation.

(i) For points i on the CCS (Γ_{CCS}), with $c_i = 1/2$ in equation (3) one has

$$\frac{1}{2} A_{k,i} = \int_{\Gamma_{CCS}} \left(\phi_i^* \frac{\partial A_k}{\partial n} - A_k \frac{\partial \phi_i^*}{\partial n} \right) d\Gamma. \quad (k = x,\ y,\ z) \tag{5}$$

(ii) For a magnetic field sensor location i, taking $c_i = 1.0$ one obtains

$$\begin{aligned} B_j - W_j^{(B)} = & \int_{\Gamma_{CCS}} \left\{ \left(L_x^j \phi_i^* \right) \frac{\partial A_x}{\partial n} - A_x \left(L_x^j \frac{\partial \phi_i^*}{\partial n} \right) \right\} d\Gamma + \int_{\Gamma_{CCS}} \left\{ \left(L_y^j \phi_i^* \right) \frac{\partial A_y}{\partial n} - A_y \left(L_y^j \frac{\partial \phi_i^*}{\partial n} \right) \right\} d\Gamma \\ & + \int_{\Gamma_{CCS}} \left\{ \left(L_z^j \phi_i^* \right) \frac{\partial A_z}{\partial n} - A_z \left(L_z^j \frac{\partial \phi_i^*}{\partial n} \right) \right\} d\Gamma. \qquad (j = r, \varphi,\ z) \end{aligned} \tag{6}$$

by applying the following operators

$$
\begin{aligned}
&L_x^r = \sin\varphi \frac{\partial}{\partial z},\ L_y^r = -\cos\varphi \frac{\partial}{\partial z},\ L_z^r = -\sin\varphi \frac{\partial}{\partial x} + \cos\varphi \frac{\partial}{\partial y},\\
&L_x^\varphi = \cos\varphi \frac{\partial}{\partial z},\ L_y^\varphi = \sin\varphi \frac{\partial}{\partial z},\ L_z^\varphi = -\cos\varphi \frac{\partial}{\partial x} - \sin\varphi \frac{\partial}{\partial y},\\
&L_x^z = -\frac{\partial}{\partial y},\ L_y^z = \frac{\partial}{\partial x},\ L_z^z = 0,
\end{aligned} \tag{7}
$$

to the portions of ϕ_i^* and $\partial\phi_i^* / \partial n$ in equation (3). Each operator in equation (7) corresponds to a term in $\mathbf{B} = \nabla \times \mathbf{A}$ with $\mathbf{A}$ expressed in Cartesian coordinates. The quantity $W_j^{(B)}$ in equation (6) represents the contributions of external coil currents to the magnetic field signal at the point i.

(iii) For a magnetic flux loop sensor location i, one also takes the value of unity for c_i.

For loops in the toroidal direction, the BIE corresponding to equation (2a) is given by

$$
\begin{aligned}
\psi^{(Tor)} - W^{(Tor)} = &\int_{\Gamma_{CCS}} \left\{ \frac{\partial A_x}{\partial n} \left(\int_0^{2\pi} \left(-R\sin\varphi \cdot \phi_i^* \right) d\varphi \right) - A_x \left(\int_0^{2\pi} \left(-R\sin\varphi \cdot \frac{\partial \phi_i^*}{\partial n} \right) d\varphi \right) \right\} d\Gamma \\
+ &\int_{\Gamma_{CCS}} \left\{ \frac{\partial A_y}{\partial n} \left(\int_0^{2\pi} R\cos\varphi \cdot \phi_i^* d\varphi \right) - A_y \left(\int_0^{2\pi} R\cos\varphi \cdot \frac{\partial \phi_i^*}{\partial n} d\varphi \right) \right\} d\Gamma.
\end{aligned} \tag{8a}
$$

Note here, it is enough to integrate only the portions related to ϕ_i^* from 0 to 2π along the loop. Similarly, the BIE corresponding to equation (2b) for loops in the poloidal direction is given by

$$
\begin{aligned}
\psi^{(Pol)} - W^{(Pol)} = &\int_{\Gamma_{CCS}} \left\{ \frac{\partial A_x}{\partial n} \left(\int_0^{2\pi} (-a\cos\varphi \sin\theta \cdot \phi_i^*) d\theta \right) - A_x \left(\int_0^{2\pi} (-a\cos\varphi \sin\theta \cdot \frac{\partial \phi_i^*}{\partial n}) d\theta \right) \right\} d\Gamma \\
+ &\int_{\Gamma_{CCS}} \left\{ \frac{\partial A_y}{\partial n} \left(\int_0^{2\pi} (-a\sin\varphi \sin\theta \cdot \phi_i^*) d\theta \right) - A_y \left(\int_0^{2\pi} (-a\sin\varphi \sin\theta \cdot \frac{\partial \phi_i^*}{\partial n}) d\theta \right) \right\} d\Gamma \\
+ &\int_{\Gamma_{CCS}} \left\{ \frac{\partial A_z}{\partial n} \left(\int_0^{2\pi} (a\cos\theta \cdot \phi_i^*) d\theta \right) - A_z \left(\int_0^{2\pi} (a\cos\theta \cdot \frac{\partial \phi_i^*}{\partial n}) d\theta \right) \right\} d\Gamma.
\end{aligned} \tag{8b}
$$

The quantities $W^{(Tor)}$ in equation (8a) and $W^{(Pol)}$ in equations (8b) are the external coil current effects on the signals of the flux loops in the toroidal and the poloidal directions respectively.

Equations (5), (6), (8a) and (8b) are discretized, coupled and can be expressed in a matrix equation form. Further, considering the 10-fold rotational symmetry of the field in the toroidal direction, the size of the matrix in the matrix equation as well as the number of unknowns can be reduced by a factor of 10 [15]. One can now solve all the values of the Dirichlet conditions

(A_x, A_y, A_z) and the Neumann conditions ($\partial A_x / \partial n, \partial A_y / \partial n, \partial A_z / \partial n$) on Γ_{CCS} in a least square sense.

2.5 Solve matrix equation

The matrix equation to be solved has the form

$$\mathbf{Dp} = \mathbf{g}, \tag{9}$$

where the solution vector $\mathbf{p}$ contains the vector potentials on the CCS and their normal derivatives. This matrix equation can be solved using the singular value decomposition (SVD) technique [16]. In this technique, the matrix $\mathbf{D}$ is decomposed as $\mathbf{D} = \mathbf{U\Lambda V}^{\mathrm{T}}$, where $\mathbf{U}$ and $\mathbf{V}^{\mathrm{T}}$ are orthogonal matrices and the symbol T denotes the matrix transpose, while $\mathbf{\Lambda}$ is a diagonal matrix with positive singular value or zero components. Basically the solution is given by $\mathbf{p} = \mathbf{V\Lambda}^{-1}\mathbf{U}^{\mathrm{T}}\mathbf{g}$, however, one can employ the Tikhonov regularization [17] to stabilize the numerical ill-posedness. In this case the stabilized solution is given by

$$\mathbf{p} = \mathbf{V}\left(\mathbf{\Lambda}^{\mathrm{T}}\mathbf{\Lambda} + \gamma \mathbf{I}\right)^{-1} \mathbf{\Lambda}^{\mathrm{T}}\mathbf{U}^{\mathrm{T}}\mathbf{g} \tag{10}$$

using the Tikhonov regularization parameter γ .

2.6 Calculate magnetic field

Once all the values of vector potential and its normal derivative on the CCS are known, the magnetic fields for arbitrary points can be calculated using the formula.

$$\begin{aligned} B_j = & \int_{\Gamma_{\mathrm{CCS}}} \left\{ \left(L_x^j \phi_i^* \right) \frac{\partial A_x}{\partial n} - A_x \left(L_x^j \frac{\partial \phi_i^*}{\partial n} \right) \right\} d\Gamma + \int_{\Gamma_{\mathrm{CCS}}} \left\{ \left(L_y^j \phi_i^* \right) \frac{\partial A_y}{\partial n} - A_y \left(L_y^j \frac{\partial \phi_i^*}{\partial n} \right) \right\} d\Gamma \\ & + \int_{\Gamma_{\mathrm{CCS}}} \left\{ \left(L_z^j \phi_i^* \right) \frac{\partial A_z}{\partial n} - A_z \left(L_z^j \frac{\partial \phi_i^*}{\partial n} \right) \right\} d\Gamma + W_j^{(B)}. \qquad (j = r, \varphi, z) \end{aligned} \tag{11}$$

2.7 Magnetic field line tracing

Once the 3-D magnetic field distribution has been obtained, the magnetic field line can be traced. In the present research, this trace is performed using the MGTRC code [18]. Magnetic fields at any points are interpolated using a three-dimensional 4th order spline function. Equations of field lines are integrated with the use of an 8-stage 6th order Runge-Kutta formulation. The profile of LCMS can then be identified following this process.

2.8 Some notes

2.8.1 About the sensor signals

In the case of a flux loop in the 3-D non-axisymmetric device, the detailed variation in vector potential along the loop is eliminated by the loop integral. Then, using only flux loop signals, it is impossible to give a proper solution for the magnetic ‘field’. In this case a least-square solution still exists and it is unique if there are a sufficient number of flux loop signals. Of course it is not the desired solution. For example, when using only flux loops in the toroidal direction, the solution must be ‘axisymmetric’. On the other hand, in the authors’ experience, the use of only field sensors in the 3-D space could give fairly acceptable solutions for the field. In the numerical examples in Section 3, where both field sensors and flux loops are considered, the flux loop signals are, so to speak, auxiliary information or constraints.

2.8.2 About the CCS modeling

From a purely mathematical point of view, the same result should be given with any size and with any shape of CCS. However, there are numerical errors in a computation. As suggested in the Appendix, the field solution given by the CCS method has no meaning inside the actual plasma. The solution inside the plasma is, so to speak, turbulence or chaos that exerts a harmful influence on the accuracy of the field profile outside the plasma. From this standpoint, a small size of CCS is a good choice to avoid the numerical instability. On the other hand, a larger cross-section of CCS, i.e., a shorter distance between the CCS surface and the sensor position is better for receiving the sensor signal information. The choice of suitable shape and size of the CCS is important to assure the accuracy of the reconstructed solution.

In the authors' experience for the JT-60, a tokamak device, the best solution is obtained when the width of the CCS is set to be 1/4 – 1/3 of the plasma width [7]. For the LHD, a helical device, however, the authors had to use a torus shape CCS having a very small diameter of cross-section, say, 0.075m to avoid a short distance from the CCS to the LCMS for all toroidal angles. This is because the shape of the poloidal cross-section of the plasma drastically changes in the toroidal direction.

2.8.3 Criteria for the analysis

The criteria for the present analysis of the field profile and its accuracy are as follows:

(i) A suitable size and shape of the CCS should be chosen for accurate and stable solutions.

(ii) The reconstructed field profile should have an acceptable accuracy in order to identify the plasma boundary and the LCMS through the field line tracing.

3. Numerical examples

One here considers the problem of modeling the non-axisymmetric plasma with a volume-averaged beta being $\langle\beta\rangle = 2.7\%$ in the LHD. The reference MHD equilibrium for this condition had been analyzed beforehand [19] using the 3-D MHD equilibrium calculation code HINT2 [20]. That is, the magnetic sensor signals and the magnetic field caused by the external coil currents are known before the analysis. The field caused by the plasma current should be reconstructed. Next, through the field line tracing, the plasma boundary and the LCMS should be found. The reconstructed results are compared with the reference solutions.

The axisymmetric, torus-shaped Cauchy condition surface (CCS) was placed within a domain that can be supposed to be inside the actual plasma. The cross section of this torus was a circle having a radius of 0.075m, of which the center was at r=3.7303m (major radius) and z=0.0m. This center is the geometrical center of the reference LCMS, which is based on the 'averaged' plasma pressure profile calculated using the HINT2 code [20]. Considering a 10-fold rotational symmetry, only a 36-deg. portion of the CCS torus was modeled and this portion was divided into 48 discontinuous quadratic boundary elements, each of which has 9 nodal points [21].

The number of unknowns is the product of numbers of nodes ($N = 48 \times 9$), components of vector potential (=3) and boundary conditions at each nodal point (=2: the Dirichlet and the Neumann conditions). Thus it becomes $6N = 2592$ in this case. Since one consumes $3N$ equations for the points i on the CCS (see equation (5)), the number of sensor signals must be larger than the remaining number of equations, i.e., $3N$. As described below, one assumes a total of 1446 sensor signals, which is larger than $3N = 1296$. Thus the problem can be solved in a least-square manner.

Figure 3 Sensor locations on the *r*-*z* plane at $\varphi = 18$ deg.

Figure 3 illustrates sensor locations on the *r*-*z* plane at the toroidal angle of 18 deg. The black dots show the 100 magnetic flux loops set in the toroidal direction, each of which is at a distance of 0.9m from the point $(r,\, z) = (3.7303m,\, 0.0m)$. The two circles depict the flux loops in the poloidal direction, which have radii of 1.0m and 1.2m respectively with the center $(r,\, z) = (3.7303m,\, 0.0m)$. A total of 26 flux loops of this type are set on 13 different *r*-*z* planes.

The white dots illustrate the positions of 40 magnetic field sensors placed on this *r*-*z* plane. They are arranged a little way outside the LCMS. A total of 440 magnetic sensors are placed on 11 different *r*-*z* planes, but they are purposely placed within the range of toroidal angle, $0° \le \varphi \le 36°$. This arrangement of sensors is identical to the case where all of the sensors are distributed carefully for the whole range $0° \le \varphi \le 360°$ in such a way that there will be no equivalent point under the 10-fold rotational symmetry.

Each of the field sensors is hypothetically assumed to detect all of the three components of magnetic field. The total number of sensor signals is then $440\times 3+100+26=1446$. The signals from these sensors had been calculated beforehand using the HINT2 code. Eventually one could solve the matrix equation (9). The Tikhonov regularization parameter in equation (10) was set to be $\gamma=1.0\times 10^{-14}$, so that the condition number, which originally exceeded 10^{15}, was reduced to about 10^{7}.

After all boundary values on the CCS were determined, the magnetic fields for arbitrary points were calculated following equation (11). The external coil effect $W_j^{(B)}$ in equation (11) had been computed beforehand using the HINT2 code. First, the magnetic field caused by only the plasma electric current, $B_j - W_j^{(B)}$, was directly provided from the CCS analysis, as will be seen in Section 3.1 and 3.2. Next, the above coil effect $W_j^{(B)}$ was added to this $B_j - W_j^{(B)}$, and then one obtained the magnetic field B_j caused by the sum of plasma current and coil current, which will be shown in Section 3.3. Both reconstructed results, $B_j - W_j^{(B)}$ and B_j, are compared respectively with the HINT2 reference solutions.

3.1 Reconstructions of sensor signals

The sensor signals discussed in this section do not include the coil current effect. Figure 4(a) shows the reproduction of signals of flux loop in the toroidal direction. The abscissa represents the original sensor signal, whereas the ordinate indicates the value reconstructed from the CCS computation. All points are about on the diagonal line ($y=x$) in the figure. This means that the reconstructed flux values show excellent agreement with the original loop signals.

In contrast, the reconstructed values of magnetic field sensor signals are not very accurate. In Figure 4(b), the points denoting B_r, B_φ and B_z scatter around the diagonal line.

One possible reason to explain the difference of accuracy between the flux loop signal and the field signal is that the magnetic field is a differential of the vector potential while the flux is an integral of the vector potential.

Figure 4 Reconstructions of sensor signals

3.2 Reconstructions of magnetic field profiles (1): Coil effect excluded

Figures 5 through 7 show examples of the magnetic field profiles when the external coil effect is excluded. These figures give the contours of the *r*-, *φ*- and z-components (B_r, B_φ and B_z) respectively of the magnetic field on the *r*-*z* plane at the toroidal angle of 18 deg. (so-called horizontal elongated cross section). In each figure, the reference solution calculated using the HINT2 code is shown on the left (Figures 5(a), 6(a) and 7(a)), while the reconstructed one obtained using the CCS method is on the right hand side (Figures 5(b), 6(b) and 7(b)). As the magnetic fields computed using the CCS method have no physical meaning inside the plasma boundary [22] (see also the Appendix), they are not drawn inside the LCMS in these figures.

Figure 5 Profiles of magnetic field B_r caused by plasma current only

Figure 6 Profiles of magnetic field B_φ caused by plasma current only

Figure 7 Profiles of magnetic field B_z caused by plasma current only

The reconstructed field profiles agree fairly well with the reference ones. Figures 5(c), 6(c) and 7(c) show the distributions of absolute error, $\varepsilon(\mathrm{T})$, which is calculated as

$$\varepsilon(\mathrm{T}) = \left|\text{Reconstructed value - Reference value}\right|, \tag{12}$$

respectively for the components of the field, B_r, B_φ and B_z. In each of these figures, the closed line indicates the LCMS. For the points outside the LCMS (1846 points out of the total of 2500 points used for drawing the figures), Table 2 also summarizes the absolute errors. No portions are found outside the LCMS where the absolute error is larger than 0.05T.

Table 2 Absolute errors in field reconstructed without considering coil effect

	B_r	B_φ	B_z
No. of points outside LCMS	1846	1846	1846
$\varepsilon < 0.01$(T)	1763 (95.5%)	1245 (67.4%)	1254 (67.9%)
$\varepsilon < 0.005$(T)	1313 (71.1%)	499 (27.0%)	579 (31.4%)
$\varepsilon < 0.001$(T)	545 (29.5%)	24 (1.3%)	130 (7.0%)
Max. error (T)	0.0249	0.0451	0.0192
Ave. error (T)	0.0035	0.0079	0.0075

Figure 8 also shows the reconstructed profile of B_r without considering the coil effect, but on the r-φ plane at $z = 0$, the so-called ‘equatorial’ plane. This figure demonstrates not only the 36-degree rotational symmetry but also the 18-degree helical symmetry of the field profile,

$$B_r(r,\ z,\ -\varphi) = -B_r(r,\ -z,\ \varphi), \tag{13}$$

the characteristics of which are peculiar to the LHD.

Figure 8 Profile of reconstructed magnetic field B_r on r-φ plane ($z = 0$)

3.3 Reconstructions of magnetic field profiles (2): Coil effect included

The coil effect was added to each of the results shown in Figures 5, 6 and 7. The relative errors of B_r, B_φ and B_z in this case, which were calculated as

$$\varepsilon\,(\%) = 100.\times \left|(\text{Reconstructed value - Reference value}) / \text{Reference value}\right|, \tag{14}$$

are summarized in table 3. The relative error is smaller than 5% in the greater part outside the LCMS. This is because the coil effect on the magnetic field is ten or more times larger than that of plasma current effect.

Table 3 Relative errors in field reconstructed after considering coil effect

	B_r	B_φ	B_z
No. of points outside LCMS	1846	1846	1846
$\varepsilon < 10\%$	1806 (97.8%)	1818 (98.5%)	1822 (98.7%)
$\varepsilon < 5\%$	1686 (91.3%)	1794 (97.2%)	1802 (97.6%)
$\varepsilon < 1\%$	1184 (64.1%)	1429 (77.4%)	1484 (80.4%)
Max. error (%)*	298.0	119.4	378.5
Ave. error (%)	2.14	1.11	3.33

*) These are caused locally by the very small values of reference fields.

3.4 Magnetic field line tracing

Two traces of magnetic field line were carried out. One was for the reference field given beforehand using the HINT2 code; the other was for the reconstructed field from the CCS analysis. Each field was the one that was caused by both plasma and coil currents. For these two fields, the starting points of the traces were set as $r = 4.30 + 0.01 n_R \ (n_R = 0, 1, \cdots, 40) \ m$, $z = 0.0m$ and $\varphi = 18°$. Each trace was terminated when the circulations reached 100 or when the field line ran out of the analytic domain under consideration.

Figure 9(a) shows the Poincaré plots of the field line on the horizontally elongated cross section ($\varphi = 18°$). The white round symbols and the red symbols are the results following the reference field and the reconstructed field, respectively. The white closed line indicates the LCMS given from the reference field. In the LHD configuration, even outside the LCMS one finds Poincaré plots which are caused by the "chaotic" field lines that reach the divertor plate after many circulations around the torus [22]. This chaotic field line region outside the LCMS is also called the "stochastic region". The reconstructed “plasma boundary” indicated in figure 9(a), which is here precisely defined as the outer surface of the stochastic region, shows a good agreement with the reference one. It is interesting to point out that even marks of the divertor legs can be found in both the reconstructed and the reference Poincaré plots.

Figure 9(b) highlights the Poincaré plots for traces originating at the same starting point $(r,\ z, \varphi) = (4.47m,\ 0.0m,\ 18°)$, which formed the LCMS when following the reference field. The solid closed line is based on the reference magnetic field, while the round symbols are the results following the reconstructed field. The former represents the LCMS clearly. The latter does not form a sharp closed surface, however, the round symbols are distributed almost along the reference LCMS.

Figure 9 Results of magnetic field line tracing

4. Conclusion and further remarks

This work is the first application of Kurihara’s CCS method to non-axisymmetric, 3-D fusion plasma. A prototype of 3-D CCS method code has been developed, in which the formulation is based on the 3-D distribution of vector potential. For magnetic field sensors and flux loops, the BIEs for x-, y- and z-components of vector potential are solved simultaneously.

In the BIE for a flux loop, only the portions related to the fundamental solution are further integrated along the loop so as to be consistent with the loop signal. The rotational symmetry, which is peculiar to LHD, is incorporated into the boundary integral formulation in order to reduce the number of unknowns.

A 3-D test calculation has been made for non-axisymmetric plasma in the LHD. Outside the LCMS the reconstructed magnetic field caused by only the plasma current agrees fairly well with the reference solution obtained using the HINT2 code, while a good agreement is observed when adding the coil current effect to the magnetic field. It is concluded that the magnetic field outside the plasma can be reconstructed with a fairly acceptable accuracy if a large number of magnetic sensors can be located outside the plasma. The magnetic field line tracing using the reconstructed field indicates the plasma boundary (the outer surface of the stochastic region) precisely and the LCMS agrees fairly well with the reference one.

The authors believe that one of the main causes of the insufficient accuracy in the reconstructed results is the huge number of unknowns required for the 3-D analysis. This causes the large condition number in the matrix equation and the loss of some information when introducing the regularization. One possible idea to resolve this situation is the additional introduction of the 18-degree "helical symmetry" (as shown in equation (13)) in order to further reduce the number of unknowns. Apart from this idea, the authors are considering the following to improve the accuracy:

(i) One should investigate the best combination of analytic conditions, e.g., the locations of various magnetic sensors as well as the arrangement and the number of nodal points on the CCS.

(ii) Guidelines need to be established for the best way of regularization, e.g., the optimized parameter for the Tikhonov regularization or for the truncated singular value decomposition [17].

(iii) One needs to examine the effect of the particular currents in the stochastic region on the reconstructed results.

(iv) Instead of the present axisymmetric CCS having a circular cross section, another idea is a 'twisted CCS' that is not axisymmetric but whose elliptic cross section rotates with the variation in vacuum vessel geometry in the toroidal direction. Independent of the toroidal angle, this CCS can keep a certain distance from its surface to the plasma boundary, so that a reduction in the numerical error can be expected. This new type of CCS is now under development in the authors' research group.

Acknowledgments

This research was performed with the support and under the auspices of the NIFS Collaboration Research Program (NIFS10KLHH308). This work was also supported by the Ministry of Education, Culture, Sports, Science and Technology, Grant-in-Aid for Scientific Research (C), 20560762, 2010.

References

[1] Strait, E.J., Fredrickson, E.D., Moret, J.M. and Takechi, M. 2008 *Fusion Science and Technology* **53** 304

[2] Lao, L.L., St. John, H., Stambaugh, R.D. and Pfeiffer, W. 1985 *Nucl. Fusion*, **25**, 1421

[3] Swain, D.W and Neilson, G.H. 1982 *Nucl. Fusion*, **22**, 1015

[4] Feneberg, W., Lackner, K. and Martin, P. 1984 *Comp. Phys. Commun*., **31**, 143

[5] Hofmann, F. and Tonetti, G. 1988 *Nucl. Fusion*, **28**, 519

[6] Kurihara, K. 2000 *Fusion Eng. Des.* **51-52** 1049

[7] Itagaki, M., Yamaguchi, S. and Fukunaga, T. 2005 *Nucl. Fusion* **45** 153

[8] Chu, M.S. and Okabayashi, M. 2010 *Plasma Phys. Control. Fusion* **52** 123001

[9] Portone, A., Villone, F., Liu, Y., Albanese, R. and Rubinacci, G. 2008 *Plasma Phys. Control. Fusion* **50** 085004

[10] Chance, M.S. 1997 *Phys. Plasmas* **4** 2161

[11] Atanasiu, C.V., Boozer, A.H., Zakharov, L.E., Subbotin, A.A. and Miron, G.I. 1999 *Phys. Plasmas* **6** 2781

[12] Hirshman. S.P., Lazarus, E.A., Hanson, J.D., Knowlton, S.F. and Lao, L.L 2004 *Phys. Plasmas* **11** 595

[13] Pustovitov, V.D. 2008 *Plasma Phys. Control. Fusion* **50** 105001

[14] Brebbia, C.A. 1978 *The Boundary Element Method for Engineers* (London: Pentech Press)

[15] Itagaki, M., Ishimaru, T. and Watanabe, K. 2010 *Proc. the 32nd International Conf. on Boundary Elements and Other Mesh Reduction Methods*, (Southampton, U.K., 2010), (WIT Press, Southampton, U.K.) p.133

[16] Press, W.H., Flannery, B.P., Teukolsky, S.A. and Vetterling, W.T. 1986 *Numerical Recipes - The Art of Scientific Computing* (Cambridge: Cambridge University Press)

[17] Hansen, P.C. 1998 *Rank-Deficient and Discrete Ill-Posed Problems – Numerical Aspects of*

Linear Inversion (Philadelphia: SIAM)

[18] National Institute for Fusion Science (Japan) 2009 *LHD Experiment Technical Guide 2009* (*http://www.lhd.nifs.ac.jp/lhd/databook_2009/LHD_technical_guide2009/pdf/LHD%20Experiment%20Technical%20Guide.pdf* *)*

[19] Seki, R., Matsumoto, Y., Suzuki, Y., Watanabe, K. and Itagaki, M. 2008 *Plasma **Fusion** Res.* **3** 016

[20] Suzuki, Y., Nakajima, N., Watanabe, K., Nakamura, Y. and Hayashi, T. 2006 *Nucl. Fusion* **46** L19

[21] Itagaki, M., Sahashi N. 1996 *J. Nucl.Sci. Eng.* **36** 7

[22] Matsumoto. Y., Oikawa, S., Watanabe, T. 2002 *J. Phys. Soc. Jpn* **71** 1684

[23] Kurihara, K. 1993 *Nucl. Fusion* **33** 399

Appendix: Validity of the hypothetical assumption of vacuum field for the plasma region

The proof shown below is written in terms of vector potential. Kurihara originally gave the proof in terms of magnetic flux in his work [23]. Now consider the domain Ω_{C-P} that is sandwiched between the plasma boundary (Γ_P) and the CCS (Γ_{CCS}).

(i) Vector potential caused by the existence of plasma current:

The BIE in this case is written in the form

$$c_i \tilde{A}_{k,i} = \int_{\Gamma_{CCS}} \left(\phi_i^* \frac{\partial A_k}{\partial n} - A_k \frac{\partial \phi_i^*}{\partial n} \right) \mathrm{d}\Gamma + \int_{\Omega_{C-P}} (\mu_0 j_k) \phi_i^* \mathrm{d}\Omega + W_{k,i} \, . \tag{A1}$$

By adding

$$\int_{\Gamma_P} \left(\phi_i^* \frac{\partial A_k}{\partial n} - A_k \frac{\partial \phi_i^*}{\partial n} \right) \mathrm{d}\Gamma - \int_{\Gamma_P} \left(\phi_i^* \frac{\partial A_k}{\partial n} - A_k \frac{\partial \phi_i^*}{\partial n} \right) \mathrm{d}\Gamma = 0 \tag{A2}$$

to the RHS of equation (A1), one obtains

$$c_i \tilde{A}_{k,i} = \int_{\Gamma_P} \left(\phi_i^* \frac{\partial A_k}{\partial n} - A_k \frac{\partial \phi_i^*}{\partial n} \right) \mathrm{d}\Gamma + W_{k,i} + c_i^{\#} \tilde{A}_{k,i}^{\#} \, , \tag{A3}$$

where the quantity $c_i^{\#} \tilde{A}_{k,i}^{\#}$ is given by

$$c_i^{\#}\tilde{A}_{k,i}^{\#} = \int_{\Gamma_{CCS}-\Gamma_P}\left(\phi_i^*\frac{\partial A_k}{\partial n} - A_k\frac{\partial \phi_i^*}{\partial n}\right)\mathrm{d}\Gamma + \int_{\Omega_{C-P}}(\mu_0 j_k)\phi_i^*\mathrm{d}\Omega\,. \tag{A4}$$

It should be noted that $c_i^{\#} = 0$ for any point outside Ω_{C-P}. Equation (A1) can then be transformed into

$$c_i\tilde{A}_{k,i} = \int_{\Gamma_P}\left(\phi_i^*\frac{\partial A_k}{\partial n} - A_k\frac{\partial \phi_i^*}{\partial n}\right)\mathrm{d}\Gamma + W_{k,i} \tag{A5}$$

that has no term related to the plasma current.

(ii) Vector potential when assuming a vacuum field for the plasma region:

The CCS method is based on the boundary integral equation for a vacuum field

$$c_iA_{k,i} = \int_{\Gamma_{CCS}}\left(\phi_i^*\frac{\partial A_k}{\partial n} - A_k\frac{\partial \phi_i^*}{\partial n}\right)\mathrm{d}\Gamma + W_{k,i}\,, \tag{A6}$$

which has no inhomogeneous term related to the plasma current. By adding

$$\int_{\Gamma_P}\left(\phi_i^*\frac{\partial A_k}{\partial n} - A_k\frac{\partial \phi_i^*}{\partial n}\right)\mathrm{d}\Gamma - \int_{\Gamma_P}\left(\phi_i^*\frac{\partial A_k}{\partial n} - A_k\frac{\partial \phi_i^*}{\partial n}\right)\mathrm{d}\Gamma = 0 \tag{A7}$$

to the RHS of equation (A6), one obtains

$$c_iA_{k,i} = \int_{\Gamma_P}\left(\phi_i^*\frac{\partial A_k}{\partial n} - A_k\frac{\partial \phi_i^*}{\partial n}\right)\mathrm{d}\Gamma + W_{k,i} + c_i^{\#}A_{k,i}^{\#} \tag{A8}$$

with

$$c_i^{\#}A_{k,i}^{\#} = \int_{\Gamma_{C-P}}\left(\phi_i^*\frac{\partial A_k}{\partial n} - A_k\frac{\partial \phi_i^*}{\partial n}\right)\mathrm{d}\Gamma\,. \tag{A9}$$

The value of $c_i^{\#}$ in equation (A9) must be zero for any point outside Ω_{C-P}. Thus one obtains

$$c_iA_{k,i} = \int_{\Gamma_P}\left(\phi_i^*\frac{\partial A_k}{\partial n} - A_k\frac{\partial \phi_i^*}{\partial n}\right)\mathrm{d}\Gamma + W_{k,i}\,. \tag{A10}$$

(iii) Conclusion

As the RHS of equation (A10) is exactly the same as the RHS of equation (A5), it is concluded that equation (A6) is identical to equation (A1), i.e., $A_{k,i} = \tilde{A}_{k,i}$. That is, at any point outside the plasma region, the vector potential calculated under the assumption of a vacuum field even for the plasma region is exactly the same as the vector potential caused by the existence of plasma current.

List of Figures

Figure 1 Extention of CCS method to a 3-D system

Figure 2 Image of magnetic sensor locations

Figure 3 Sensor locations on the *r*-*z* plane at $\varphi = 18$ deg.

Figure 4 Reconstructions of sensor signals

Figure 5 Profiles of magnetic field B_r caused by plasma current only

Figure 6 Profiles of magnetic field B_φ caused by plasma current only

Figure 7 Profiles of magnetic field B_z caused by plasma current only

Figure 8 Profile of reconstructed magnetic field B_r on r-φ plane ($z = 0$)

Figure 9 Results of magnetic field line tracing

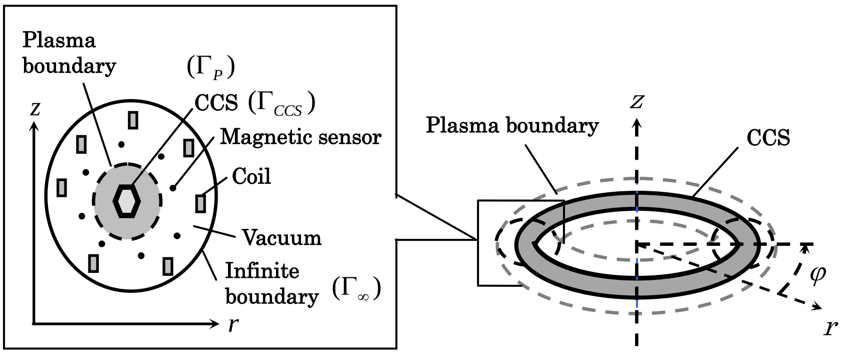

Figure 1 Extention of CCS method to a 3-D system

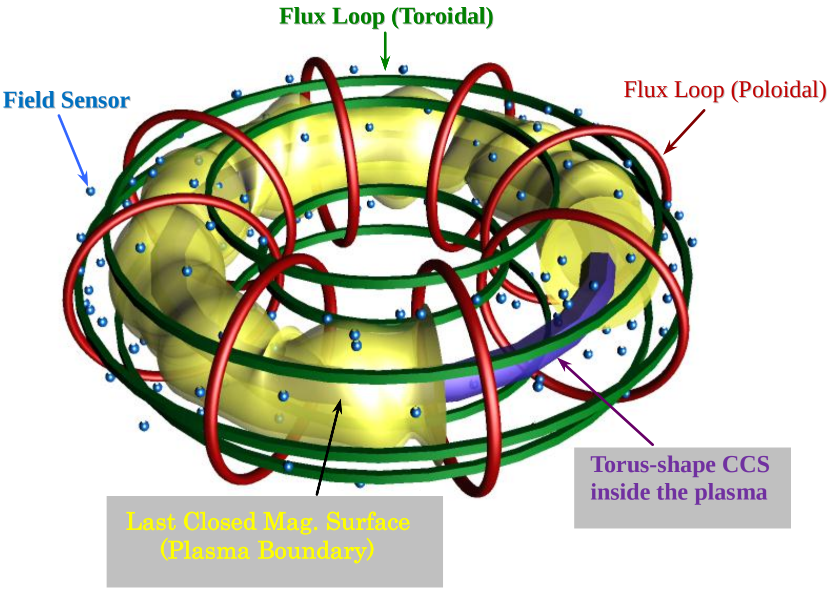

Figure 2 Image of magnetic sensor locations

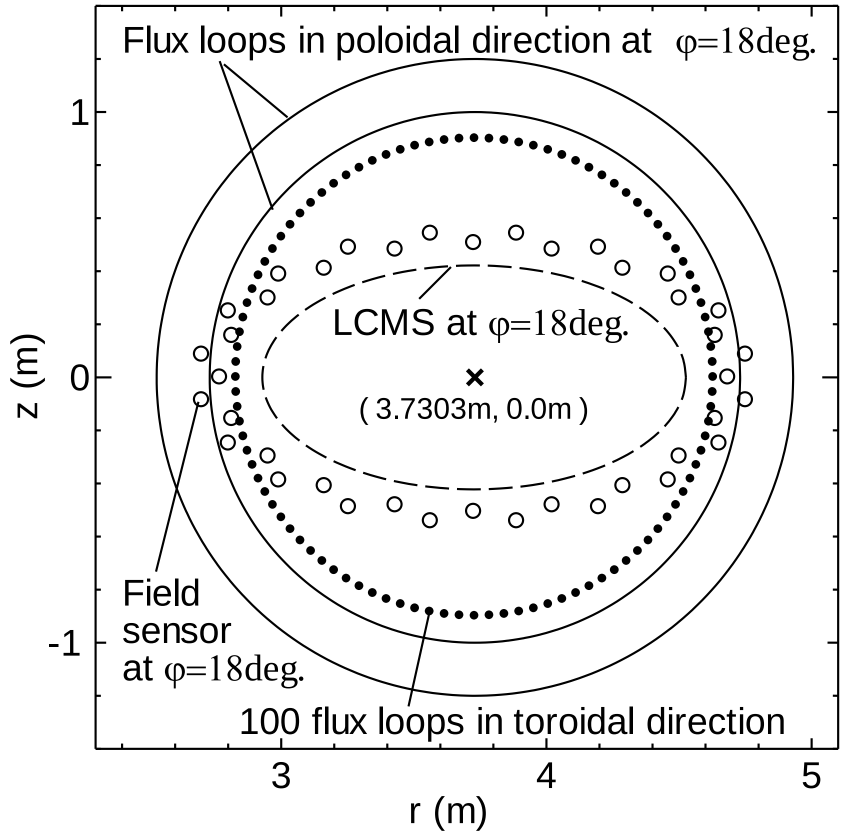

Figure 3 Sensor locations on the *r*-*z* plane at $\varphi = 18$ deg.

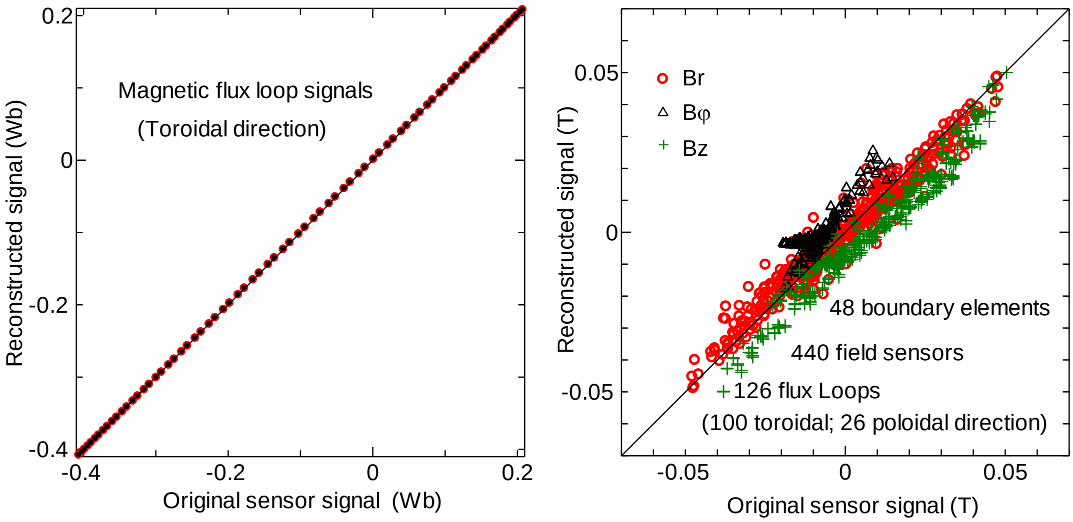

(a) Toroidal loop signals

(b) Field sensor signals

Figure 4 Reconstructions of sensor signals

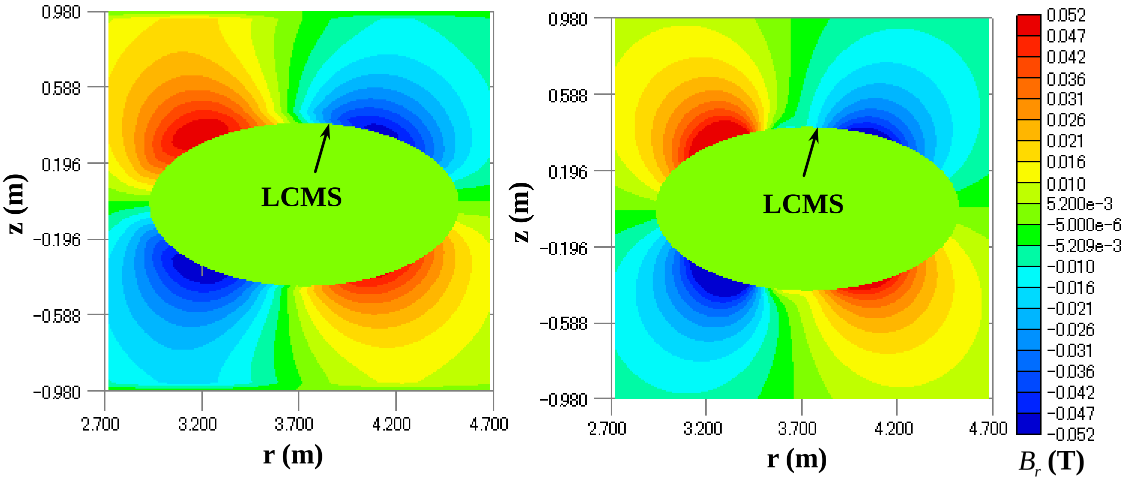

(a) Reference (HINT2)

(b) Reconstructed (CCS method)

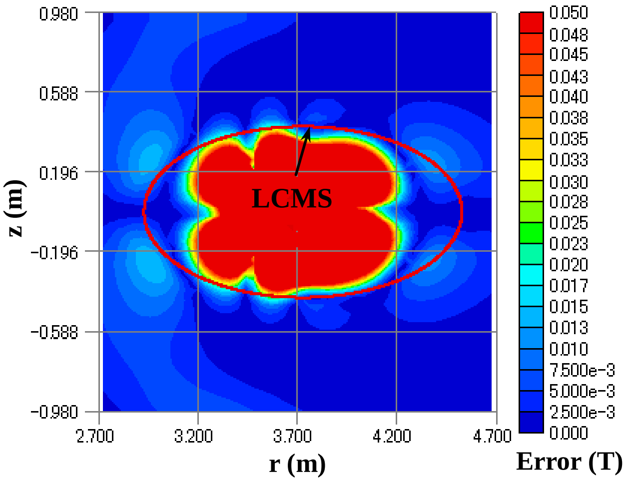

(c) Absolute error

Figure 5 Profiles of magnetic field B_r caused by plasma current only

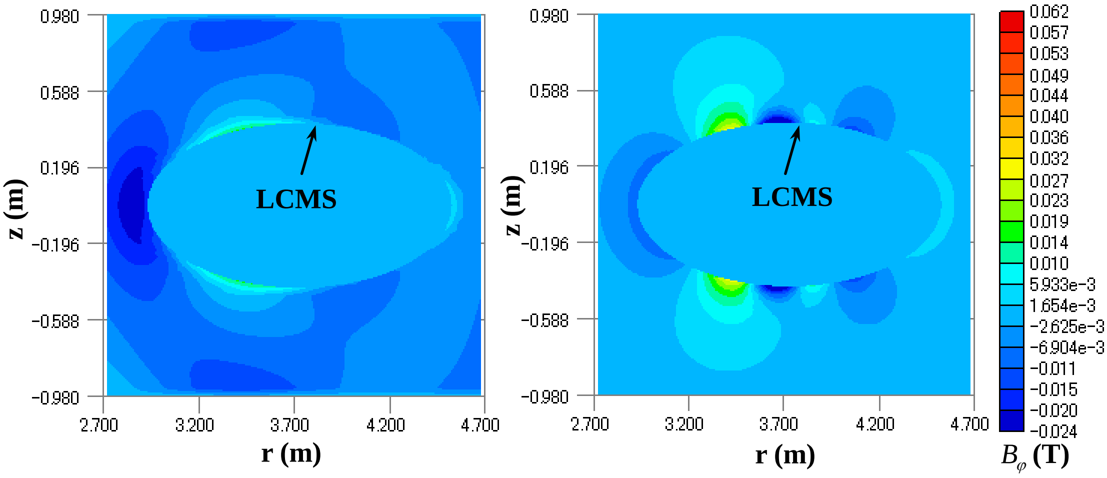

(a) Reference (HINT2)

(b) Reconstructed (CCS method)

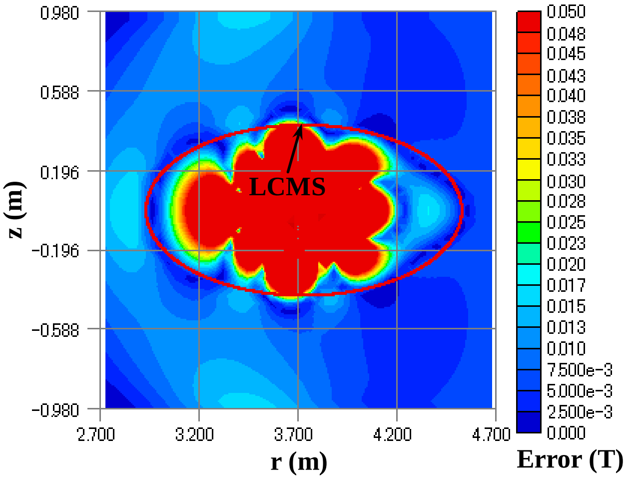

(c) Absolute error

Figure 6 Profiles of magnetic field B_φ caused by plasma current only

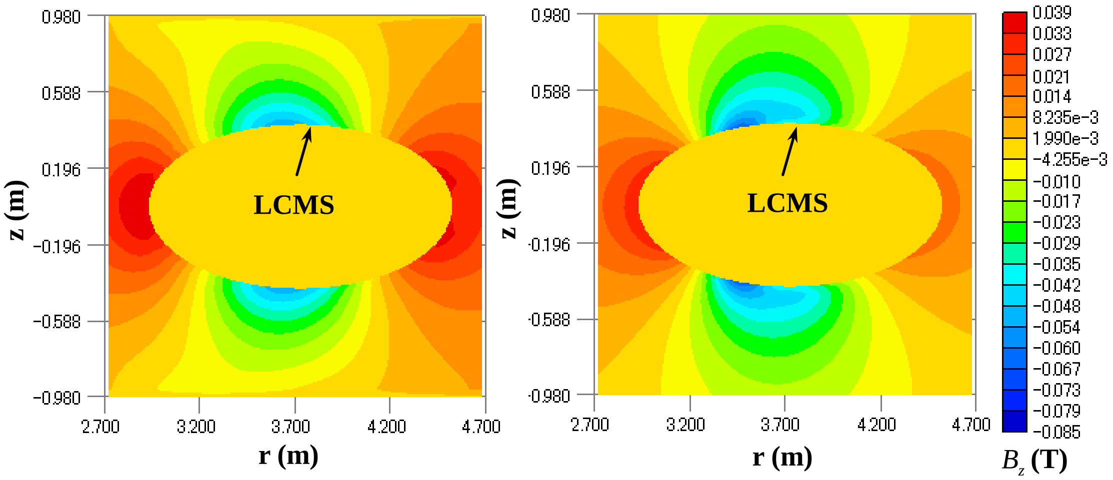

(a) Reference (HINT2) (b) Reconstructed (CCS method)

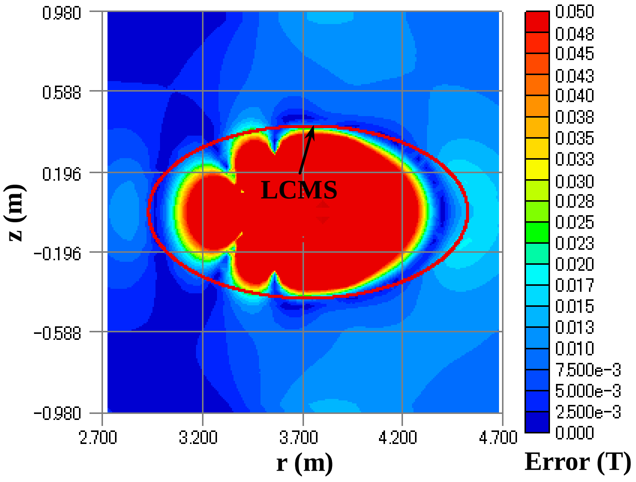

(c) Absolute error

Figure 7 Profiles of magnetic field B_z caused by plasma current only

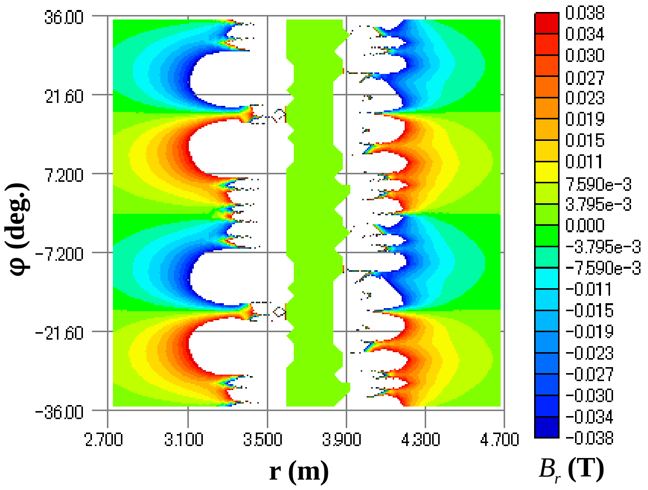

Figure 8 Profile of reconstructed magnetic field B_r on r-φ plane ($z = 0$)

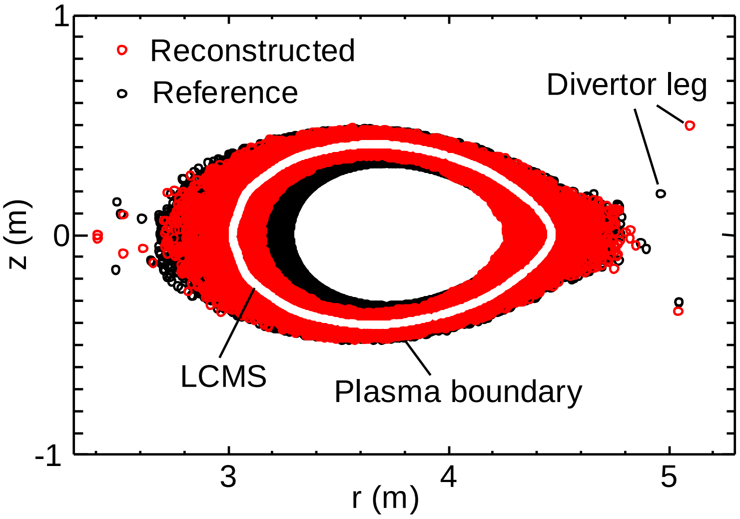

(a) Peripheral region

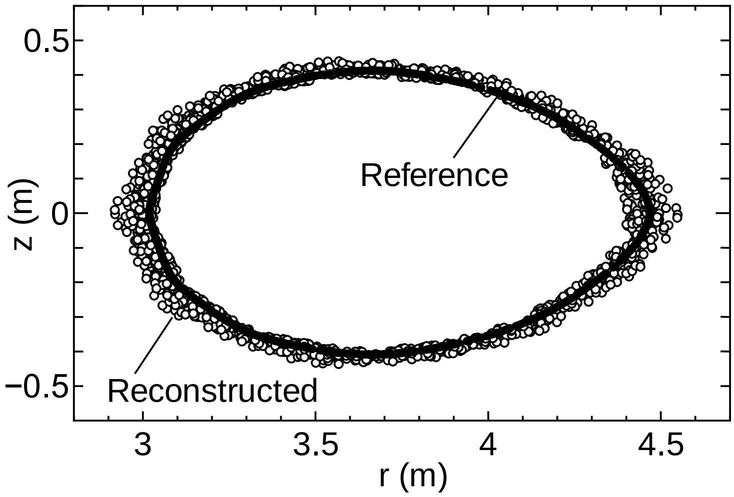

(b) LCMS

Figure 9 Results of magnetic field line tracing